

A microfluidic platform with permeable walls for the analysis of vascular and extravascular mass transport

C. Manneschi¹ · R. C. Pereira¹ · G. Marinaro¹ · A. Bosca¹ · M. Francardi¹ · P. Decuzzi¹ 

Received: 1 May 2016 / Accepted: 5 July 2016 / Published online: 18 July 2016
© Springer-Verlag Berlin Heidelberg 2016

Abstract The interface between the blood pool and the extravascular matrix is fundamental in regulating the transport of molecules, nanoparticles and cells under physiological and pathological conditions. In this work, a microfluidic chip is presented comprising two parallel microchannels connected laterally via an array of high aspect ratio micropillars, constituting the permeable vascular membrane. A double-step lithographic process combined with a replica molding approach is employed to realize 80 different arrays of micropillars exhibiting three cross-sectional geometries (rectangular, elliptical and curved); two orientations (normal and parallel) with respect to the flow; and a variety of width and gap sizes, respectively, ranging from 10 to 20 μm and 2 to 5 μm . As compared to conventional rectangular structures, the curved pillars provide higher bending stiffness, lower adhesive interactions, and smaller intra-channel separation distances. Specifically, 10- μm -wide curved pillars, laying parallel to the flow, offered the highest mechanical stability. To assess vascular permeability, the extravascular channel was filled with a hyaluronic acid hydrogel, while fluorescent Dextran molecules and calibrated polystyrene beads were injected in the vascular channel. Membrane permeability was observed to reduce

with the molecular weight of Dextran and diameter of the beads, ranging from about 6×10^{-5} to 2×10^{-5} cm/s for 40 and 250 kDa Dextran and up to zero for 1.5 μm beads. The presented data demonstrate the potential of the proposed microfluidic chip for analyzing the vascular and extravascular mass transport, over multiple spatial and temporal scales, in a variety of diseases involving differential permeation across vascular walls.

Keywords Vascular interface · Permeable walls · Transport · Microfabrication · Microfluidic · Extravascular matrix

1 Introduction

The interface between the blood pool and the extravascular matrix plays a major role in both physiological and pathological conditions. Vascular walls contribute in regulating the tissue permeability of nutrients, waste products and drug molecules (Jain and Stylianopoulos 2010; Kang et al. 2014; Mathura et al. 2015; Warboys et al. 2010); modulating the trafficking of immune cells (Ley et al. 2007); controlling the deposition of platelets for wound healing and blood clot formation (Sorrentino et al. 2015); determining the intravasation and extravasation of cancer cells and the progressive invasion of circulating monocytes into atherosclerotic plaques (Gay and Felding-Habermann 2011; Libby et al. 2009). Furthermore, vascular permeability and the expression of endothelial receptor molecules affect the accumulation of systemically administered nanoconstructs in diseased tissues, such as neoplastic lesions and atherosclerotic plaques (Aryal et al. 2013; Key et al. 2015; Kim et al. 2014). This has been documented in vivo via sophisticated techniques based on intravital video microscopy,

M. Francardi and P. Decuzzi are co-senior authors.

Electronic supplementary material The online version of this article (doi:10.1007/s10404-016-1775-5) contains supplementary material, which is available to authorized users.

✉ P. Decuzzi
paolo.decuzzi@iit.it

¹ Laboratory of Nanotechnology for Precision Medicine, Fondazione Istituto Italiano di Tecnologia, Via Morego 30, 16163 Genoa, Italy

where vascular and trans-endothelial transport of cells and nanoconstructs can be detected in real time, in a living animal. A few examples are given by the study of the progressive accumulation of fluorescently labeled nano- and microparticles into neoplastic tissues (Jain and Stylianopoulos 2010); the infiltration of monocytes into infarcted areas (Jung et al. 2013); the deposition of circulating tumor cells into the cerebral microvasculature (Kienast et al. 2010); and the formation and dissolution of blood clots. (Voros et al. 2015) Although such sophisticated in vivo studies provide biophysical conditions closer to the human phenotype, they suffer of economical, temporal and ethical constraints, particularly in the screening of novel drugs and rational design of nanoconstructs. Furthermore, in vivo studies do not allow for a precise control of the major biophysical governing parameters, such as vascular permeability and architecture, flow and shear rates, extravascular matrix composition.

Multiple in vitro assays have been proposed for studying the vascular transport and trans-endothelial trafficking of cells and nanoconstructs. The transwell migration assay is perhaps the most well-known and prototypical example. (Chen 2005) It comprises two chambers (upper and lower) separated by a permeable, *porous membrane* coated by a confluent layer of endothelial cells. Under proper conditions, cells and nanoconstructs deposited in the upper chamber would migrate into the lower chamber by crossing the endothelial monolayer. At the bottom of the lower chamber, a second monolayer of tissue cells is cultured. Generally, the membrane has a thickness of about 10 μm and pores with a diameter ranging from several hundreds of nanometers to a few microns. This conventional transwell architecture does not support any dynamic flow, any real-time monitoring of migration processes via optical microscopy, and introduces a significant separation between the upper and lower chambers limiting any direct endothelial-to-tissue cell interactions. More recently, microfluidic systems have been integrated with the transwell concept whereby polycarbonate porous membranes are sandwiched between two overlaid microfabricated channels. (Abaci et al. 2015; Booth and Kim 2012; Griep et al. 2013; Jang and Suh 2010; Sticker et al. 2015) Essentially, these are transwells where different flow conditions can be readily imposed within the microchannels but still do not allow for the real-time monitoring of migration processes or direct cell-to-cell interactions. Alternative designs realize channels running parallelly one to each other, on the same plane, which are separated by a *micropillar array*, generating micron-sized gaps or short channels, formed in the common lateral walls (Hamza and Irimia 2015; Lamberti et al. 2014; Lee et al. 2007; Menon et al. 2015; Prabhakar-pandian et al. 2013; Yeon et al. 2012; Zervantonakis et al. 2012). This geometry allows for a direct, real-time imaging

of the migration process across the lateral gaps, laying on the same optical plane as the microchannels. However, in these configurations, micropillars are either shorter than the height of the channels, thus altering locally the flow and biological microenvironment uniformity, or tend to be mechanically unstable as their aspect ratios increase. (Sharp et al. 2004) Therefore, widths and gaps for the array of pillars often fall within tens of microns resulting in a moderate control in permeability and lack of any biologically significant cell-to-cell interaction across microchannels. Both strategies, *porous membrane* and *micropillar array*, have been used for reproducing in vitro the blood brain barrier (Booth and Kim 2012; Griep et al. 2013; Yeon et al. 2012); liver sinusoids (Lee et al. 2007) and other vascular districts (Huh et al. 2012; Lee et al. 2015; Stucki et al. 2015), for various mass transport studies (Hamza and Irimia 2015; Lamberti et al. 2014; Menon et al. 2015; Zervantonakis et al. 2012).

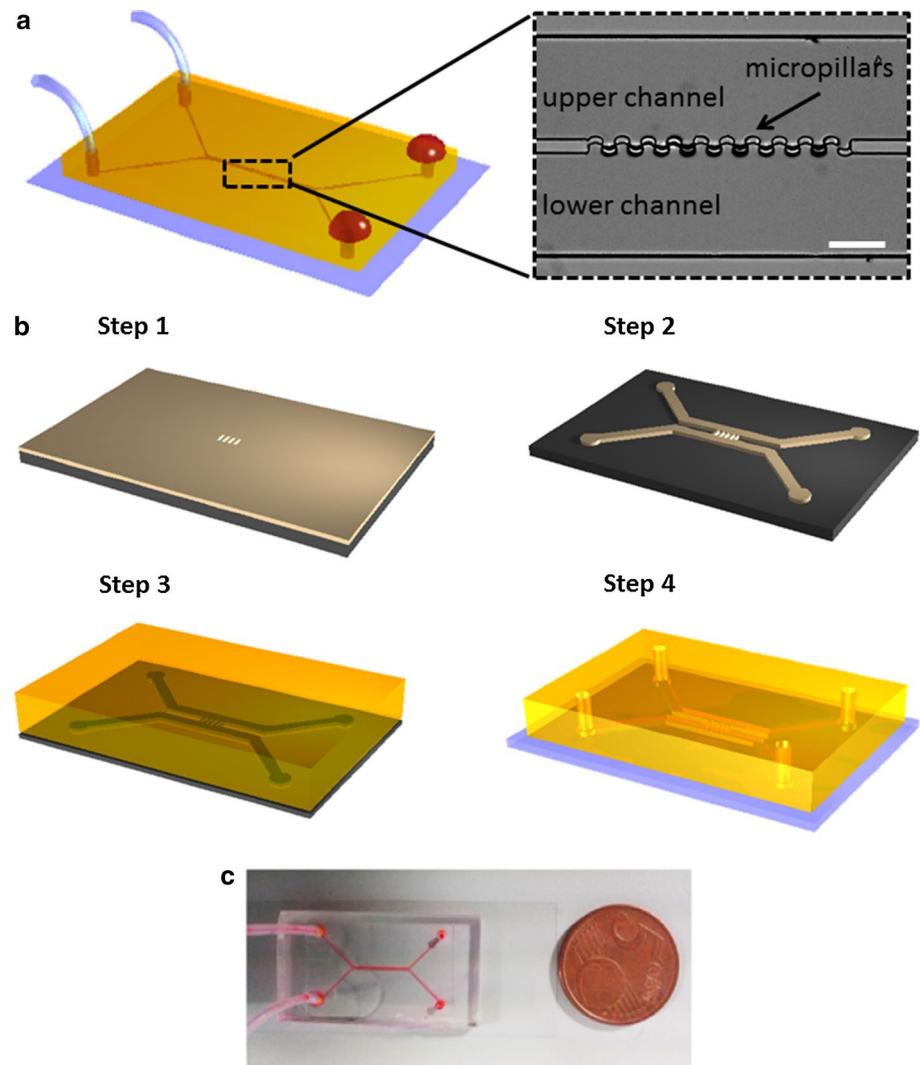
In this work, a direct Bosch etching process and a double-step replica molding approach are combined to fabricate two parallel microchannels connected laterally via an array of micropillars—the *permeable membrane*. The double-step approach allows for a precise control of the micropillar geometry and orientation. Thus, here, pillars with a rectangular, elliptical and curved cross sections are considered, with different relative spacing and oriented normally or parallelly to the flow. Eight different configurations are tested with the objective of identifying the micropillar array with the highest mechanical stability and lower separation distance between the parallel microchannels. Optical microscopy can be readily used to capture both the fast vascular transport and the slow trans-vascular migration of cells and nanoconstructs. After assessing the mechanical stability of the micropillars, the transport of fluorescent spherical beads is performed to characterize the geometrical permeability of the membrane under different biological conditions.

2 Materials and methods

2.1 Materials

Silicon (Si) wafer (4''-P-doped— $\langle 100 \rangle$ — $10\text{--}20 \Omega/\text{cm}^2$ — $525 \mu\text{m}$ thick, from Si-Mat) was used for the realization of the hard templates. During the fabrication of the templates, patterns were transferred from the optical mask onto the resist layer and then from the resist onto a thin Chromium (Cr 99.95 %, Kurt J. Lesker Company) layer, that was used as hard mask for the ICP-RIE etching process. AZ5214E (Microchem) was chosen as resist due to its image reversal capability, and the solvent AZ726MF (Microchem) was used as developer. Chromium etching was performed

Fig. 1 Microfluidic chip with permeable walls. **a** Schematic and SEM image of the chip. The upper and lower microchannels have a width of $200\ \mu\text{m}$ and a height of $50\ \mu\text{m}$. Microchannels are connected via a $500\ \mu\text{m}$ long array of micropillars (scale bar is $100\ \mu\text{m}$). **b** Schematic of the fabrication process consisting in a double-step lithographic approach (etching of the pillars and etching of the whole chip) and replica molding process (PDMS replica and chip assembling on a glass slide). **c** Image of the final chip connected to syringe pumps via silanic tubing



by using a commercial Cr etchant (Chrome etch 18, OSC OrganoSpezialChemie GmbH).

As all the structures were patterned on the silicon wafer, 1H,1H,2H,2H-Perfluoro-octyl-trichloro-silane ($125\ \mu\text{l}$, Alfa Aesar) was used to produce an anti-adhesive layer on the template. PDMS replicas of the Si template were produced by using a pre-polymer solution of Sylgard 182 (Dow Corning). Glass coversheets (No. 1.5H, Deckaläser) were used in order to obtain close microfluidic chips.

Spherical particles of different sizes (Fluoresbrite™ Carboxy NYO $0.2\ \mu\text{m}$ microspheres, Fluoresbrite™ Carboxylate YG $0.75\ \mu\text{m}$ microspheres, Fluoresbrite™ Carboxylate YO $1.75\ \mu\text{m}$ microspheres and Fluoresbrite™ Carboxylate YG $10\ \mu\text{m}$ microspheres from Polyscience; fluorescent polystyrene blue $5\ \mu\text{m}$ beads from Phosphorex) were used in the permeability test of the membranes. For the study of permeability without HA, particles were packaged as $0.25\ \%$ solution. In the experiments performed using the HA hydrogel, particles with diameter of $0.2\ \mu\text{m}$ were

packaged as $0.0025\ \%$ aqueous suspension, while 0.75 and $1.75\ \mu\text{m}$ large particles were packaged as $0.00025\ \%$ aqueous suspension. Prior to their use, solutions were vortexed for $10\ \text{s}$ to avoid formation of aggregates.

Eagle's minimum essential medium (EMEM) was purchased from ATCC®, (ATCC®, USA), phosphate-buffered saline (PBS) and fetal calf serum were purchased from Life Technologies™ (Eugene, OR, USA). Hyaluronic acid Corgel™ BioHydrogel (TS-NaHy) was acquired from Lifecore Biomedical (Lifecore Biomedical, LLC, Chaska, USA).

2.2 Fabrication of microfluidic chips

The chips, whose layout is shown in Fig. 1a, were fabricated by using a replica molding approach. All the process is described in Fig. 1b. It mainly consisted in two lithographic steps for the creation of a silicon master that was then replicated by PDMS (Fig. 1c). Si master template was

derived by using a top-down approach whereby the negative pattern of the chip was transferred on a Silicon (Si) wafer. First, a 50-nm Chromium (Cr) layer was deposited on the lapped surface. The thin Cr layer acts as the hard mask for transferring the negative pattern on the Si wafer. Since the etching rate of the Bosch process depends on the surface of the pattern, a double lithographic step was necessary to obtain structures with homogenous depths. With this aim, two optical masks were realized by direct laser writing (DLW6000, Heidelberg): the first mask with the positive pattern of pillars; the second mask with the negative pattern of the channels. In order to realign the two patterns, a series of markers were included in the masks. Given the double nature of the patterns (i.e., positive and negative), the AZ5214E was chosen as a photoresist due to its ability to be used in both, positive and negative processes. AZ5214E was spin-coated for 60 s at 4000 rpm to obtain a 1.4- μm -thick layer on the Cr surface. Then, the sample pre-baked on a hot-plate at 110 °C for 1 min to remove any residual solvent from the resist. Using a mask aligner for the optical lithography (SUSS, MicroTec), the mask (A) was impressed on the AZ5214E with a dose of 80 mJ. Then, the resist was developed for 50 s in AZ726MF and rinsed in deionized water. A commercial Cr etchant was used to transfer the pattern into the Cr layer by means of a 50-s-long wet etching followed by rinse in deionized water. The AZ5214E layer from the non-exposed surface was then removed by acetone coupled with sonication (US), followed by oxygen (O_2) plasma (Plasma System Tucano, Gambetti). Finally, the wafer was placed in an Inductive Coupled Plasma-Reactive Ions Etching (SI 500, SENTECH Instruments GmbH) where a Bosch process was performed to transfer the patterns onto the Si wafer. Due to the high precision required with depth, the ICP-RIE process was optimized resulting in an etching rate of 330 nm for cycle. Each cycle was composed of a deposition phase (C_4F_8 150 sccm, SF_6 5 sccm, with a pressure of 5 Pa, 15 W of RF, ICP Power of 700 W, for 6 s) and an etching phase (SF_6 129 sccm, Ar 30 sccm, with a pressure of 1 Pa, 40 W of RF, ICP Power of 800 W, for 9 s). After 15 cycles, the pillar pattern was transferred over the Si wafer for a depth of $\sim 5 \mu\text{m}$. The spurious of C_4F_8 layer, which was generated by the ICP-RIE process, was removed by O_2 plasma treatment.

The resulting silicon wafer, with the pillar pattern already transferred, prepared for the second step: transferring of the channel pattern. AZ5214E was spin-coated over the residual Cr layer and pre-baked on hot-plate at 110 °C for 1 min in order to have a thickness of $\sim 2 \mu\text{m}$. After the realignment of the channel mask with the pattern on the pillars, the photoresist was exposed by using a dose of 95 mJ. In this step, the resist was used in image reversal mode. Therefore, the wafer was placed again on a hot-plate for post-baking at 120 °C for 120 s and subjected to a flood

exposure with dose of 300 mJ. The development was again performed with the same solvent and method used for the pillars. The channel pattern was transferred into the Cr, and the photoresist stripped from the surface as described above. At this point, both pillars and channel patterns are co-present on Cr layer and only pillars on the Si wafer. Performing 150 cycles of the optimized Bosch process, both patterns were transferred in the Si layer up to a depth of $\sim 50 \mu\text{m}$. After cleaning the template from the residual C_4F_8 via O_2 plasma treatment, all the Cr was removed by the specific wet etching. In order to promote the subsequent release of a PDMS replica, the silicon master was silanized after chrome etching. The master was treated with O_2 plasma and an antistiction layer was deposited on it, specifically leaving both the master and a drop of silane inside desiccator for 1 h.

PDMS replicas of the Si template were produced by using a pre-polymer solution of Sylgard 182. It was prepared by mixing the base with the curing agent with a ratio (w/w) 10:1. After mixing, the solution was incubated in a vacuum chamber for degassing. Then, it was casted on the silicon template and after a second step of degassing, it was cured in an oven at 60 °C for 4 h. After baking, the whole system was cooled down to $-20 \text{ }^\circ\text{C}$ for nearly 1 h before the peeling-off of the PDMS. This step helps in peeling-off the PDMS stamp without damaging the membrane.

2.3 Study on the stability of pillars

Three silicon templates with 2D array of membranes, made of pillars with different geometries, size and gap, were fabricated and reproduced with PDMS following the same procedure as reported previously. After the peeling-off, replicas are observed both by means of an upright microscope (DM5500 B, Leica) in bright field mode and by scanning electron microscope (JSM-6490LV, JEOL and Helios Nanolab 650, FEI CompanyTM). SEM images were acquired after a pre-treatment that consists in the coating of the PDMS stamps with 50 nm of gold. All the images were acquired by secondary electrons imaging (SEI) mode. Low magnification and high magnification SEM images were obtained with accelerating voltage of 15 and 5 kV, respectively.

2.4 Fluidic setup

PDMS molds were punched to create four holes with 1.5 mm of diameter for the handling of the fluids. Replicas were treated with O_2 plasma and bonded with a glass coversheet. Once the bonding was achieved, the top of the microfluidic chip underwent another O_2 plasma treatment in order to induce a hydrophilic behavior of the surface. Experiments of permeability of the membrane were

performed by depositing a single drop of 10 μl at 30 min from the last O_2 plasma treatment. A flow toward the three outlets was induced by capillary forces. Particles dynamics in the proximity of the membrane were observed by acquiring images at 5 fps via a fluorescent inverted microscope (Leica DMI6000 B equipped with high speed camera Leica DFC360 FX). 200 nm particles were acquired by using a filter cube Cy3. Larger particles were detected in bright field.

CorgelTM hyaluronic acid hydrogel was prepared according to supplier instructions (Lifecore Biomedical LLC, Chaska, USA) with minor adjustments. In brief, polymer was dissolved in horseradish peroxidase in PBS (10 U/ml) solution provided by the supplier to obtain 10 mg/ml final concentration solution. Polymer solution was then mixed with RPMI completed medium, and afterward hydrogel formation was initiated by addition of hydrogen peroxide (H_2O_2) with a final ratio of 1/25 (v/v). In our study, we have used the CorgelTM polymer with 1.5 % tyramine substitution degree.

A drop of 50 μl of HA was put on the inlet of the extravascular channel just after the mixing with hydrogen peroxide and aspired by means of a syringe pump. Suction with flow velocity of 50 $\mu\text{l}/\text{min}$ was applied to the extravascular channel in order to promote the complete filling with HA, while suction of 100 $\mu\text{l}/\text{min}$ was applied to the vascular outlet to avoid bubble formation at the interface between the gel and the membrane. During the optimization of the fluidic setup, gel was visualized by adding 200 nm large fluorescent microparticles to the mixture. As soon as the extravascular compartment was filled, the syringe pump was turned off and a drop with particles was positioned on one of the vascular reservoirs and inertial flow with particle was observed. Particles dynamics in the proximity of the membrane was detected by acquiring images at 10 fps via a fluorescent inverted microscope for time-lapse imaging (Eclipse Ti-E, Nikon) with FITC and TxRed filters.

3 Results and discussion

3.1 Fabrication of microfluidic chips

The microfluidic chips comprise two microchannels (upper and lower channels), each with one inlet and one outlet, connected laterally via an array of micropillars constituting the so called *permeable membrane*. A schematic representation of the chip and a scanning electron microscopy (SEM) image of the central portion of the chip with the micropillar array are displayed in Fig. 1a. The microchannels have a rectangular cross section with a width of 200 μm and a height of 50 μm . The separation wall in between the two channels is 25 μm wide. The central array of micropillars is 500 μm long in the main flow direction.

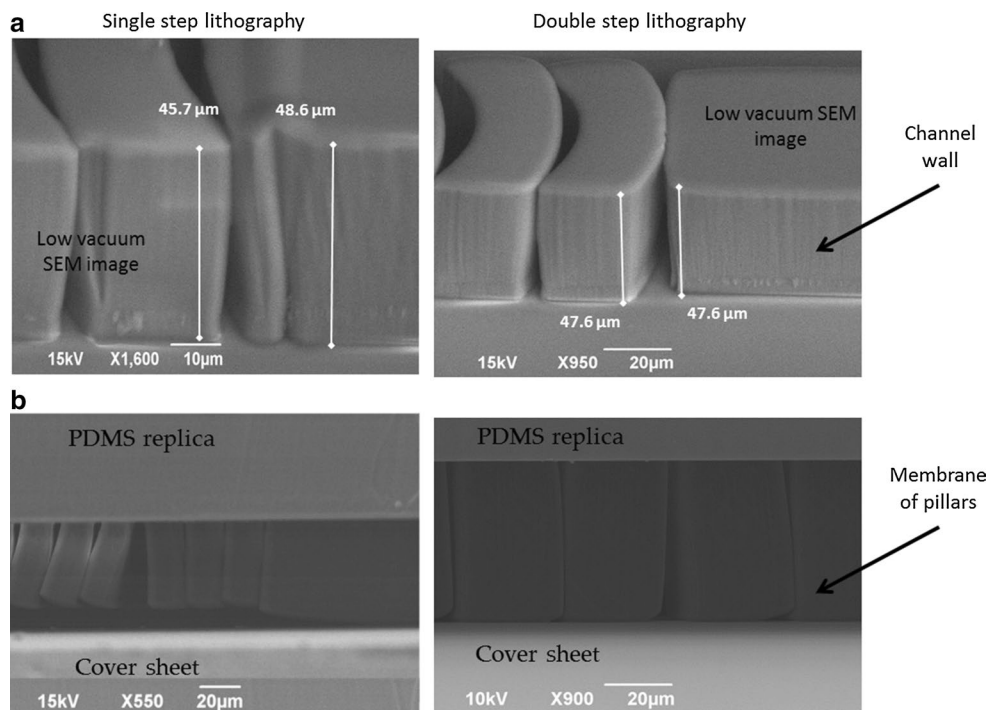
The chip is fabricated in PDMS using a combination of direct Bosch etching and replica molding approach, as depicted in Fig. 1b. The original silicon master template was produced via two subsequent lithographic steps. First, the array of micropillars (*permeable membrane*) was directly etched on the master template (step 1, in Fig. 1b) by using a Bosch process. Then, the actual geometries of the upper and lower channels were realized on the same template, upon precise fixing of reference marks (step 2, in Fig. 1b). The resulting silicon template, after silanization, was covered by PDMS, baked in oven for 4 h at 60 $^\circ\text{C}$ to produce the polymeric replica (step 3, in Fig. 1b). Finally, the PDMS replica was peeled off the original master template and, after an oxygen plasma treatment, was bonded to a glass slide to realize the actual microfluidic chip (step 4, in Fig. 1b). Inlets and outlets were generated into the PDMS replica by using punchers of proper size and shape. Then, outlets were connected to a syringe pump via polyethylene tubes for flow dynamics and particle injection. A photograph of the final chip is shown in Fig. 1c.

Note that the direct etching of patterns on the silicon wafer, via a Bosch process, allowed the realization of micropillars with higher aspect ratios than conventional approaches based on photoresist (SU-8 for instance) etching (Boesel et al. 2010). However, the Bosch process suffers of aspect ratio-dependent etching: the higher is the aspect ratio of the structure and the lower is their etching rate. Therefore, a single lithographic step approach would have led to PDMS replica with uneven structures, as long as there is a significant difference in aspect ratios. Indeed, this is the case of the present chip, where micropillars have a higher aspect ratio than the microchannel walls. Therefore, in the present case, a single lithographic step would have led to micropillars shorter than the microchannel walls. This is clearly demonstrated in Fig. 2, where SEM images of the micropillar array obtained via a single and double-step are presented, before and after bonding the PDMS replica on a glass slide. Note the significant difference in height among the micropillars and the channel side wall and the large opening of $\sim 3 \mu\text{m}$ originated between the tip of the pillars and the glass slide. Such uneven etching and difference in heights cannot be tolerated in chips where membrane permeability should be accurately controlled and modulated. Therefore, the double-step lithographic exposure, first for the pillars (step 1, in Fig. 1b) and then for the channels (step 2, in Fig. 1b), was the sole feasible approach for obtaining well aligned and organized micropillars.

3.2 Pillar geometry and mechanical stability

The micropillars are a crucial component of the microfluidic chips because they are responsible for the selective

Fig. 2 Details of the array of pillars constituting the permeable membrane. **a** SEM images of the membrane of pillars before bonding with a glass slide for the single (left) and double-step (right) lithography approaches. **b** SEM images of the membrane of pillars after bonding with the glass slide. Note the difference in height between pillars and side walls of the microchannels in the single step (left bottom) as compared to the double-step (right bottom) lithographic process



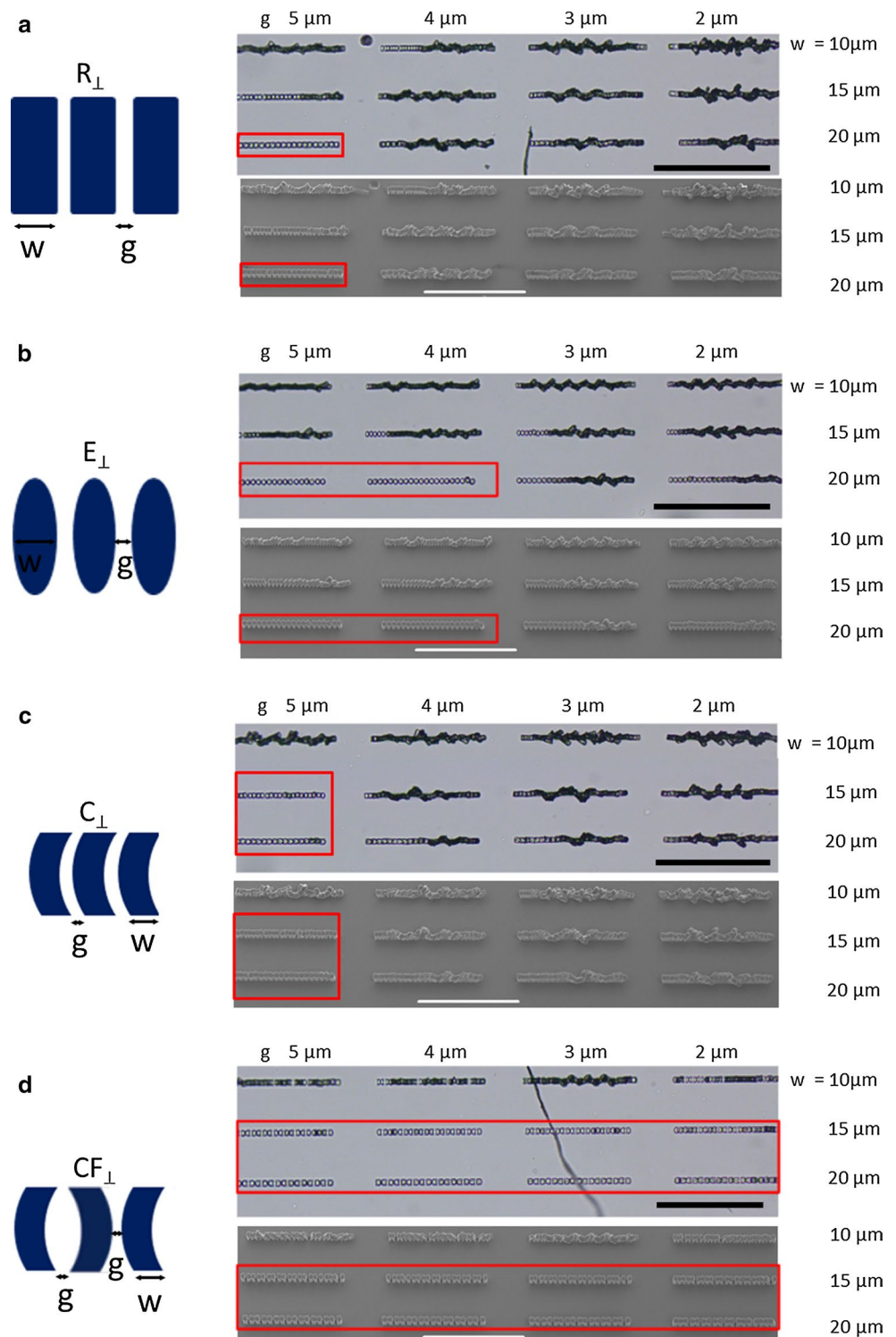
permeability of the membrane. Pillars should be as high as the channel walls ($50 \mu\text{m}$) and present narrow gaps ($<5 \mu\text{m}$). Such slender structures often incur into mechanical collapse due to colloidal interactions arising at the interface between adjacent pillars or between pillars and the bottom of the chip. In order to control as precisely as possible the gaps in mechanically stable membranes, four different parameters were specifically modulated, namely (1) the geometry of the micropillar cross section (rectangular, elliptical and curved); (2) the micropillar orientation with respect to the flow direction (normal or parallel); (3) the lateral width (w); and (4) the gap (g). The geometry and orientation of micropillars is represented schematically in Fig. S1, together with the nomenclature used throughout this manuscript.

A single silicon template was etched to replicate a 2D array of different micropillars. The pillar geometry, orientation, width and gap were systematically changed, with w ranging from 10 to $20 \mu\text{m}$ and g ranging from 2 to $5 \mu\text{m}$. This led to 80 different configurations of micropillar arrays. Note that the length and the height of the micropillars were fixed to be 25 and $50 \mu\text{m}$, respectively, to ensure their alignment with the side channel walls in the microfluidic chip. Two main groups were identified: membranes with micropillars normal and parallel to the flow. In the first group, there were rectangular (R_{\perp}), elliptical (E_{\perp}), curved (C_{\perp}) and curved flipped (CF_{\perp}) pillars (4 geometries). Curved pillars were designed to have a nominal radius of curvature of $17.5 \mu\text{m}$. By rotating and changing the separation distance between adjacent pillars, membrane with different

geometrical and stability properties were generated: curved (C_{\parallel}), curved flipped (CF_{\parallel}), curved overlapped (CO_{\parallel}) and curved shifted (CS_{\parallel}) (4 geometries). For all mechanical stability test, at least three replicas were considered and no significant difference was documented among repetitions.

Figure 3 shows optical (upper box) and SEM (lower box) images of micropillars for the different configurations in the orientation normal to the flow (a total of 48 arrays of micropillars). Rectangular pillars (R_{\perp}) were all upright and stable only at $w = 20 \mu\text{m}$ and $g = 5 \mu\text{m}$. For smaller gaps and lateral width, the micropillars tended to collapse on each other. Indeed, smaller widths w reduce the bending stiffness of the pillars and smaller gaps g increase the interfacial adhesive interaction, both favoring mechanical collapse (see Supporting Information). Pillars with an elliptical cross section (E_{\perp}) showed a slightly higher stability demonstrating no collapse for $w = 20 \mu\text{m}$ and $g = 5$ and $4 \mu\text{m}$. Although the bending stiffness of the elliptical pillars is slightly lower as compared to the rectangular pillars (see Supporting Information), the non-uniform gap of the elliptical pillars leads to significantly lower interfacial adhesive interaction, thus favoring the E_{\perp} over R_{\perp} configuration. C_{\perp} structures were also more stable than R_{\perp} demonstrating no collapse at $w = 20$ and $15 \mu\text{m}$ and $g = 5 \mu\text{m}$. Note that the C_{\perp} pillars have a larger bending stiffness as compare to R_{\perp} and E_{\perp} (see Supporting Information). However, given their orientation, the colloidal adhesive interactions are similar to that of R_{\perp} and definitely higher than E_{\perp} . Therefore, C_{\perp} pillars are still stable at a smaller w but cannot tolerate a lower g . Following

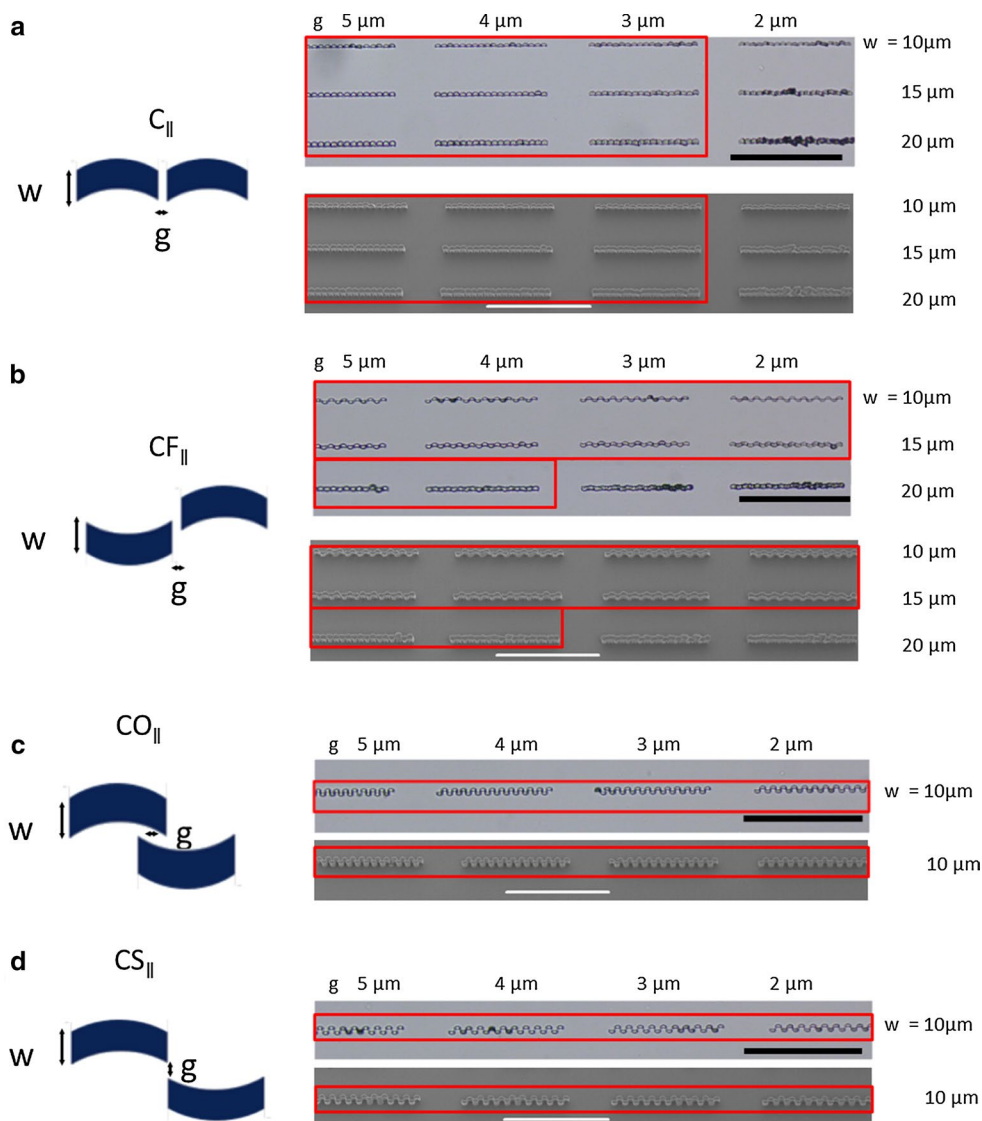
Fig. 3 Mechanical stability for the array of pillars. Optical and SEM images of the array of pillars for different geometries, gaps g and width w . Pillars are oriented normally to the flow



the above reasoning, not surprisingly the most stable structures were CF_{\perp} pillars. These arrays of micropillars appeared to be mechanically stable over a wider range of w , namely 15 and 20 μm , and for all tested gaps g . This result should be attributed to the higher bending stiffness of the curved pillars, as compared to the rectangular ones,

and to the lower adhesive interactions over the curved surface due to the larger average gap. The CF_{\perp} configuration combines the benefits of the stiffer C_{\perp} and lower adhesive E_{\perp} (see Supporting Information). However, lateral collapse of the pillars—shoulders over shoulders—may also occur in this configuration, as shown in Fig. S2.

Fig. 4 Mechanical stability for the array of pillars. Optical and SEM images of the array of pillars for different geometries, gaps g and width w . Pillars are oriented parallel to the flow



In order to better support and foster interactions among the adjacent microchannels, the width w of the micropillar arrays should be reduced below $15 \mu\text{m}$. This required to change the pillar orientation from normal to parallel to the flow, and to select only curved pillar geometries. The new arrays of micropillars are presented in Fig. 4, with optical and SEM images as before, for a total of 32 different configurations. Notably, for all considered configurations (C_{\parallel} ; CF_{\parallel} ; CO_{\parallel} ; CS_{\parallel}), the minimum width and gap for stable pillars is reduced to 10 and $2 \mu\text{m}$, respectively. Although the integrity of the membrane is preserved for every value of g and w , lateral collapse between adjacent pillars can occur in the C_{\parallel} and CF_{\parallel} configurations (Fig. S3). In the CO_{\parallel} configuration, mechanical collapse produces rather regular small fenestrations at the base of the pillars. Note that for this configuration, the minimum width of $10 \mu\text{m}$ for the pillars is imposed

in that larger separations would prevent the curved pillars to be aligned with the side walls of the microchannels. Finally, the CS_{\parallel} configuration appeared as the most stable preventing uncontrolled contact between adjacent micropillars and with small gaps at the pillars edge that would facilitate cell-to-cell interactions between the two microchannels.

In Fig. 5, SEM images of three types of micropillar membranes are presented, namely the configuration R_{\perp} , with $w = 20 \mu\text{m}$ and $g = 5 \mu\text{m}$ (Fig. 5a), the configurations CO_{\parallel} and CS_{\parallel} with $w = 10 \mu\text{m}$ and $g = 3 \mu\text{m}$ (Fig. 5b, c). Note that for configurations R_{\perp} and CO_{\parallel} , the top of the pillars are in partial contact, reducing even more the nominal gaps at the tip of the pillars. Differently, for the CS_{\parallel} configuration, the separation distance between the pillars is more uniform along the height of the pillars with no major adhesion on the sides.

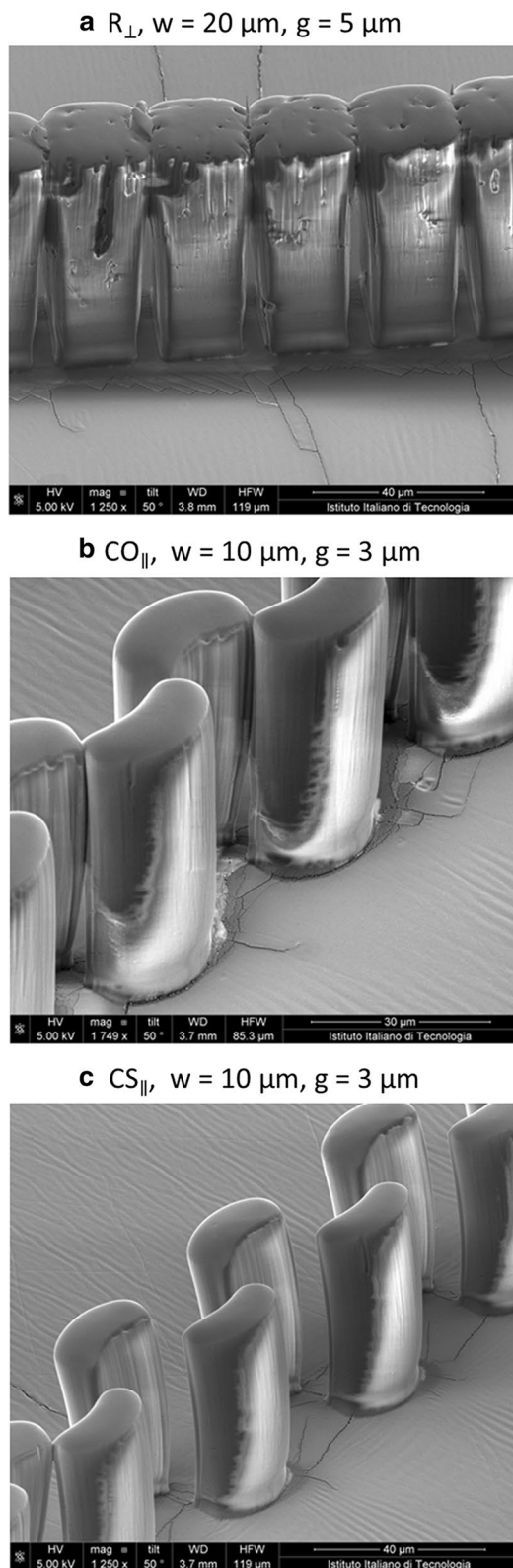


Fig. 5 Details of the array of pillars. SEM images of the pillar membranes made of **a** rectangular R_{\perp} , **b** curved overlapped CO_{\parallel} and **c** curved shifted CS_{\parallel} pillars. Note that the R_{\perp} and CO_{\parallel} structures tend to collapse on each other laterally. Differently, the CS_{\parallel} pillars are mechanically more stable

3.3 Membrane permeability test

Fluorescent Dextran molecules (40 and 250 kDa in molecular weight), nanoparticles and microparticles were employed for testing the permeability of the micropillar membranes. In a first set of experiments, the characteristic diameter of the particles was set to 200 nm, 5 and 10 μm . Particles were dispersed in DI water (0.25 % in volume) and perfused in the chip from the upper channel inlet. The vascular dynamics of the particles was monitored using an epifluorescent microscope (Fig. 6 and Supporting Movies). As expected, the smallest particles (200 nm) crossed all four tested membranes (R_{\perp} , CF_{\parallel} , CO_{\parallel} , CS_{\parallel}), giving a uniform reddish coloration in the upper and lower channels. On the other hand, the 5 μm particles, and even more the 10 μm particles, formed large clots on the upper channel side of the membrane (inlet flow). For the 5 μm particles, the clogging was rapid and more significant with the R_{\perp} configuration, less significant with the CO_{\parallel} and CS_{\parallel} , and negligible for the CF_{\parallel} configuration. This was completely permeable to 5 μm particles. All micropillar membranes were not permeable to 10 μm particles. This data confirmed that CO_{\parallel} and CS_{\parallel} are mechanically stable membranes, with a particle cutoff size of at least 5 μm , which is comparable to platelets and small circulating cells. Importantly, the curved micropillar membranes, oriented parallel to the flow, offer smaller intra-channel gaps (5 μm width) as compared to the R_{\perp} configuration (20 μm width). This is particularly important in biological applications where cells, seeded on the two opposite sides of the membrane, would need to communicate by developing tight junctions. For conventional membranes, such as the R_{\perp} , these junctions would have to be several microns long or the body of the cells would have to deform across narrow gaps. Differently, with the curved geometries parallel to the flow, a more biologically relevant configuration of the cells and gap junction development could be readily realized.

In order to decrease even more the particle cutoff size to the sub-micrometer regime and enhance biomimicry, a hydrogel of hyaluronic acid (HA) was injected in the lower channel. Upon cross linking, the HA solution formed a solid gel. Since HA is highly expressed in tumor extracellular matrices, the resulting HA hydrogel was used to mimic the extravascular compartment in the microfluidic chip (Scott 1992; Toole and Slomiany 2008). The progressive filling of the lower chamber with HA is shown in Fig. 7a and Supporting Movies. For this experiment, the CS_{\parallel} array of pillars were used, with $w = 10 \mu\text{m}$ and $g = 3 \mu\text{m}$. The small contact angle ($<90^{\circ}$) formed at the PDMS/gel interface suggests that chip filling is facilitated by capillary force suction. Moreover, no gel was observed in the upper channel, possibly due to the interplay between capillary forces and the small intra-pillar gaps. As it appears from Fig. 7a, the HA

Fig. 6 Transport experiments for nanoparticles in microfluidic chips with different pillar membranes. Spherical fluorescent polystyrene beads are injected through the upper channel and their dynamics within the chip is monitored in real time via optical microscopy (flow direction is from *left to right*). Nanoparticles of different diameter are used, namely 200 nm, 5 and 10 μm (Scale bar is 50 μm)

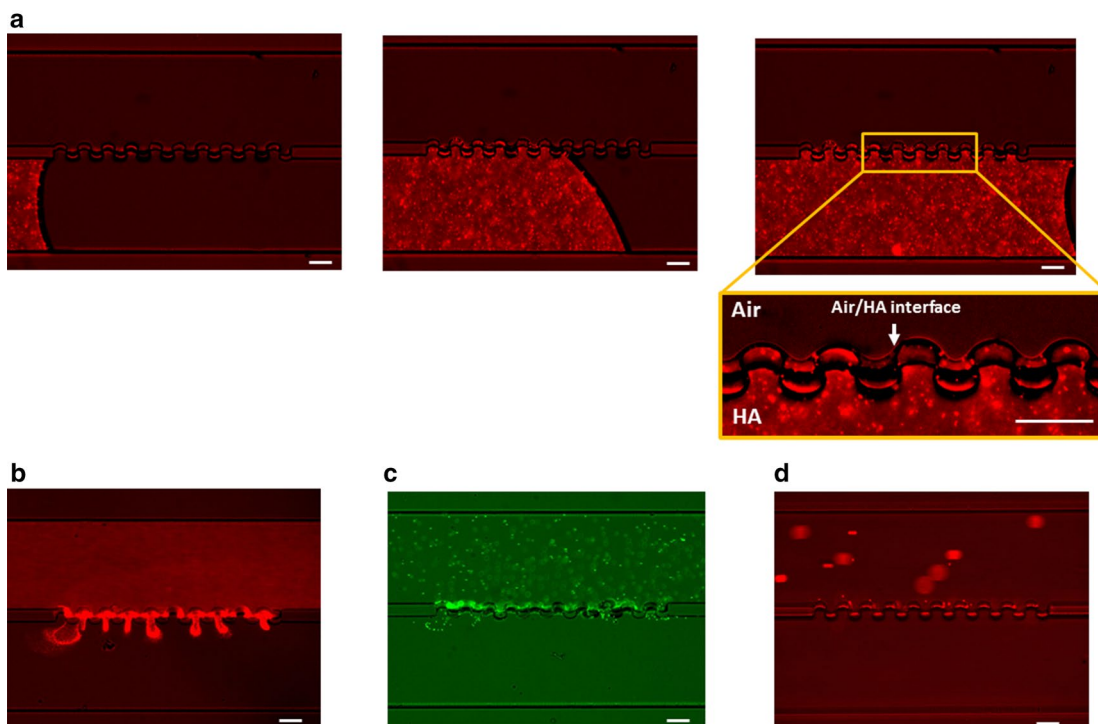
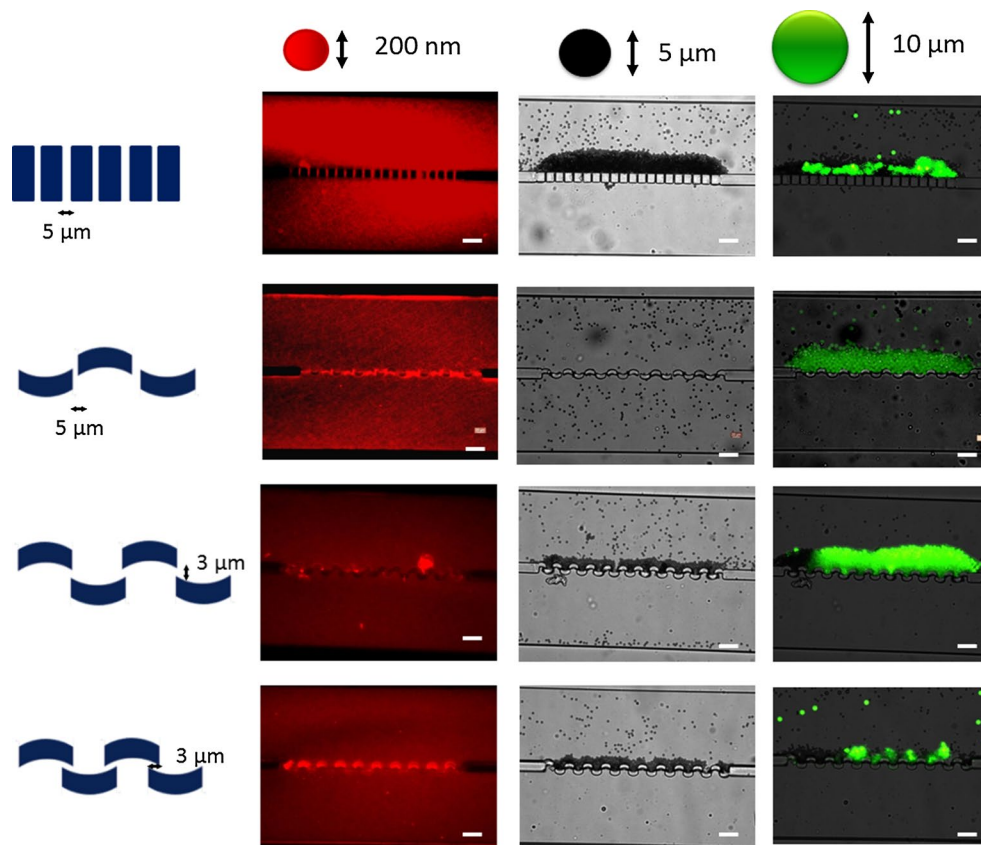


Fig. 7 Transport experiments for nanoparticles in microfluidic chips filled with hyaluronic acid. **a** The lower chamber of the chip is progressively filled with hyaluronic acid, introduced from *left to right*. **b–d** Spherical fluorescent polystyrene beads are injected through the

upper channel and their dynamics within the chip is monitored in real time via optical microscopy (flow direction is from *left to right*). Nanoparticles of different diameter are used, namely **b** 200 nm, **c** 750 nm and **d** 1.5 μm (Scale bar is 50 μm)

gel adhered to the pillars and halted just at the interface with the upper channel, which was filled with air.

Under this more biologically relevant configuration, the permeability tests were performed with smaller beads, precisely exhibiting diameters of 200 nm, 0.75 and 1.75 μm and Dextran molecules. Figure 7b–d shows images taken from full movies (see Supporting Movies) monitoring the real-time transport process. As expected, the presence of HA in the lower channel decreased the permeability in the extravascular compartment. Only the 200 nm particles were capable of penetrating deeper, for about 50 μm , within the hydrogel. A smaller portion of 0.75 μm particles accumulated at the periphery of the gel, in a so called perivascular position, whereas the larger 1.75 μm were accumulating only at the vascular interface without any significant penetration into the lower chamber. Upon injection of 40 and 250 kDa FITC-Dextran, both molecules were observed to diffuse within the HA hydrogel (extravascular compartment), as shown in Fig. S4. Notably, the fluorescent signal in the HA hydrogel associated with the 40 kDa Dextran is brighter and more spread than that observed for the larger Dextran molecules (250 kDa). By post-processing the fluorescent images, the actual permeability to Dextran was estimated to be of about 6×10^{-5} and 2×10^{-5} cm/s for the 40 and 250 kDa molecules, respectively (Fig. S4).

Furthermore, preliminary tests were performed on growing different types of cells within the microfluidic chip. In particular, Human Umbilical Vein Endothelial Cells (HUVECs) were cultured in the upper channel (vascular compartment) of the microfluidic chip reaching confluency within 4 days, as demonstrated by VE-cadherins staining (Fig. S5), whereas U87-MG cells of human glioblastoma multiforme were efficiently cultured within a HA gel in the lower channel (extravascular compartment) of the microfluidic chip (Fig. S6).

4 Conclusions

A double-step lithographic approach combined with replica molding was used to fabricate microfluidic chips with permeable walls resembling the interface between the blood pool and the extravascular matrix. The permeable wall was obtained via an array of micropillars interposed within the side walls of two parallel microchannels, laying on the same plane. The modular fabrication process allowed to realize 80 different micropillar configurations, exhibiting three different pillar cross-sectional geometries (rectangular, elliptical and curved); 2 different orientations (parallel and normal to the flow); and a variety of width and gap sizes. The mechanical stability of all 80 different micropillar configurations was tested experimentally identifying, in particular, for each pillar geometry the minimum width and gap preventing

any lateral collapse. Curved pillars oriented parallelly to the flow, either overlapped (CO_{\parallel}) or slightly shifted (CS_{\parallel}), provided the best stability with a minimum width of 10 μm and a gap of 2 μm . Over the most conventional rectangular geometry, these curved pillars offered a higher mechanical stability, due to the higher bending stiffness and lower adhesive interactions, and a lower separation distance between the two adjacent microchannels, supporting potentially a more natural cell-to-cell interaction across the vascular wall.

Spherical fluorescent polystyrene beads with a precise diameter were injected into the upper channel of the microchip and their permeation across the micropillar membrane into the lower channel was continuously monitored via optical microscopy. Large beads of 5 and 10 μm were mostly confined into the upper channel and eventually ended up clogging the permeable membrane. Differently, small fluorescent beads of 200 nm in diameter uniformly colored both the upper and lower channels demonstrating a rapid permeation across the vascular walls with a nominal gap size of 3 μm . Subsequently, a solution of hyaluronic acid was infused into the lower channel and crosslinked to generate a uniform, solid hydrogel resembling the extravascular matrix. Under this condition, the permeability of 200 nm, 0.75 and 1.5 μm beads across the membrane was significantly reduced, as compared to the free hyaluronic acid case. The penetration depth of the beads into the hydrogel reduced progressively with their size, from about 50 μm for the 200 nm beads to nearly zero for the 1.5 μm beads which just adhered to the vascular interface. Small macromolecules, such as FITC-Dextran of 40 and 250 kDa, were observed to diffuse deeper within the HA gel returning permeability values of about 6×10^{-5} and 2×10^{-5} cm/s, respectively.

It should be here emphasized that the geometry of the microchannels, the hydrodynamic conditions, and the architecture of the extravascular matrix can be readily modified during the fabrication and assembly of the chip to provide a variety of biologically relevant experimental conditions. This together with the presented data demonstrate the potential of the proposed microfluidic system for studying the vascular and extravascular transport of molecules, nanoparticles and cells, over multiple temporal and spatial scales.

Acknowledgments This project was supported by the European Research Council under the European Union's Seventh Framework Programme (FP7/2007-2013)/ERC Grant Agreement No. 616695 and by the AIRC Investigator Grant 2015 Id. 17664.

References

- Abaci HE, Gledhill K, Guo ZY, Christiano AM, Shuler ML (2015) Pumpless microfluidic platform for drug testing on human skin equivalents. *Lab Chip* 15:882–888. doi:10.1039/c4lc00999a

- Aryal S, Key J, Stigliano C, Ananta JS, Zhong M, Decuzzi P (2013) Engineered magnetic hybrid nanoparticles with enhanced relaxivity for tumor imaging. *Biomaterials* 34:7725–7732. doi:[10.1016/j.biomaterials.2013.07.003](https://doi.org/10.1016/j.biomaterials.2013.07.003)
- Boesel LF, Greiner C, Arzt E, del Campo A (2010) Gecko-inspired surfaces: a path to strong and reversible dry adhesives. *Adv Mater* 22:2125–2137. doi:[10.1002/adma.200903200](https://doi.org/10.1002/adma.200903200)
- Booth R, Kim H (2012) Characterization of a microfluidic in vitro model of the blood-brain barrier (mu BBB). *Lab Chip* 12:1784–1792. doi:[10.1039/c2lc40094d](https://doi.org/10.1039/c2lc40094d)
- Chen HC (2005) Boyden chamber assay. *Methods Mol Biol* 294:15–22
- Gay LJ, Felding-Habermann B (2011) Contribution of platelets to tumour metastasis. *Nat Rev Cancer* 11:123–134. doi:[10.1038/nrc3004](https://doi.org/10.1038/nrc3004)
- Griep LM et al (2013) BBB ON CHIP: microfluidic platform to mechanically and biochemically modulate blood-brain barrier function. *Biomed Microdevices* 15:145–150. doi:[10.1007/s10544-012-9699-7](https://doi.org/10.1007/s10544-012-9699-7)
- Hamza B, Irimia D (2015) Whole blood human neutrophil trafficking in a microfluidic model of infection and inflammation. *Lab Chip* 15:2625–2633. doi:[10.1039/c5lc00245a](https://doi.org/10.1039/c5lc00245a)
- Huh D et al (2012) A human disease model of drug toxicity-induced pulmonary edema in a lung-on-a-chip microdevice. *Sci Transl Med* 4:159147. doi:[10.1126/scitranslmed.3004249](https://doi.org/10.1126/scitranslmed.3004249)
- Jain RK, Stylianopoulos T (2010) Delivering nanomedicine to solid tumors. *Nat Rev Clin Oncol* 7:653–664. doi:[10.1038/nrclinonc.2010.139](https://doi.org/10.1038/nrclinonc.2010.139)
- Jang KJ, Suh KY (2010) A multi-layer microfluidic device for efficient culture and analysis of renal tubular cells. *Lab Chip* 10:36–42. doi:[10.1039/b907515a](https://doi.org/10.1039/b907515a)
- Jung K et al (2013) Endoscopic time-lapse imaging of immune cells in infarcted mouse hearts. *Circ Res* 112:891–899. doi:[10.1161/CIRCRESAHA.111.300484](https://doi.org/10.1161/CIRCRESAHA.111.300484)
- Kang H, Cancel LM, Tarbell JM (2014) Effect of shear stress on water and LDL transport through cultured endothelial cell monolayers. *Atherosclerosis* 233:682–690. doi:[10.1016/j.atherosclerosis.2014.01.056](https://doi.org/10.1016/j.atherosclerosis.2014.01.056)
- Key J et al (2015) Soft Discoidal polymeric nanoconstructs resist macrophage uptake and enhance vascular targeting in tumors. *ACS Nano* 9:11628–11641. doi:[10.1021/acs.nano.5b04866](https://doi.org/10.1021/acs.nano.5b04866)
- Kienast Y, von Baumgarten L, Fuhrmann M, Klinkert WE, Goldbrunner R, Herms J, Winkler F (2010) Real-time imaging reveals the single steps of brain metastasis formation. *Nat Med* 16:116–122. doi:[10.1038/nm.2072](https://doi.org/10.1038/nm.2072)
- Kim Y et al (2014) Probing nanoparticle translocation across the permeable endothelium in experimental atherosclerosis. *Proc Natl Acad Sci USA* 111:1078–1083. doi:[10.1073/pnas.1322725111](https://doi.org/10.1073/pnas.1322725111)
- Lamberti G, Prabhakarandian B, Garson C, Smith A, Pant K, Wang B, Kiani MF (2014) Bioinspired microfluidic assay for in vitro modeling of leukocyte–endothelium interactions. *Anal Chem* 86:8344–8351. doi:[10.1021/ac5018716](https://doi.org/10.1021/ac5018716)
- Lee PJ, Hung PJ, Lee LP (2007) An artificial liver sinusoid with a microfluidic endothelial-like barrier for primary hepatocyte culture. *Biotechnol Bioeng* 97:1340–1346. doi:[10.1002/bit.21360](https://doi.org/10.1002/bit.21360)
- Lee JS, Romero R, Han YM, Kim HC, Kim CJ, Hong JS, Huh D (2015) Placenta-on-a-chip: a novel platform to study the biology of the human placenta. *J Matern-Fetal Neonatal Med*. doi:[10.3109/14767058.2015.1038518](https://doi.org/10.3109/14767058.2015.1038518)
- Ley K, Laudanna C, Cybulsky MI, Nourshargh S (2007) Getting to the site of inflammation: the leukocyte adhesion cascade updated. *Nat Rev Immunol* 7:678–689. doi:[10.1038/nri2156](https://doi.org/10.1038/nri2156)
- Libby P, Ridker PM, Hansson GK, Leducq Transatlantic Network on A (2009) Inflammation in atherosclerosis: from pathophysiology to practice. *J Am Coll Cardiol* 54:2129–2138. doi:[10.1016/j.jacc.2009.09.009](https://doi.org/10.1016/j.jacc.2009.09.009)
- Mathura RA, Russell-Puleri S, Cancel LM, Tarbell JM (2015) Hydraulic conductivity of smooth muscle cell-initiated arterial cocultures. *Ann Biomed Eng*. doi:[10.1007/s10439-015-1421-5](https://doi.org/10.1007/s10439-015-1421-5)
- Menon NV, Chuah YJ, Phey S, Zhang Y, Wu Y, Chan V, Kang Y (2015) Microfluidic assay to study the combinatorial impact of substrate properties on mesenchymal stem cell migration. *ACS Appl Mater Interfaces* 7:17095–17103. doi:[10.1021/acsami.5b03753](https://doi.org/10.1021/acsami.5b03753)
- Prabhakarandian B, Shen MC, Nichols JB, Mills IR, Sidoryk-Wegrzynowicz M, Aschner M, Pant K (2013) SyM-BBB: a microfluidic Blood Brain Barrier model. *Lab Chip* 13:1093–1101. doi:[10.1039/c2lc41208j](https://doi.org/10.1039/c2lc41208j)
- Scott JE (1992) Supramolecular organization of extracellular matrix glycosaminoglycans, in vitro and in the tissues. *FASEB J* 6:2639–2645
- Sharp KG, Blackman GS, Glassmaker NJ, Jagota A, Hui CY (2004) Effect of stamp deformation on the quality of microcontact printing: theory and experiment. *Langmuir* 20:6430–6438. doi:[10.1021/la036332+](https://doi.org/10.1021/la036332+)
- Sorrentino S, Studd JD, Medalia O, Tanuj Sapra K (2015) Roll, adhere, spread and contract: structural mechanics of platelet function. *Eur J Cell Biol* 94:129–138. doi:[10.1016/j.ejcb.2015.01.001](https://doi.org/10.1016/j.ejcb.2015.01.001)
- Sticker D, Rothbauer M, Lechner S, Hehenberger MT, Ertl P (2015) Multi-layered, membrane-integrated microfluidics based on replica molding of a thiol-ene epoxy thermoset for organ-on-a-chip applications. *Lab Chip* 15:4542–4554. doi:[10.1039/c5lc01028d](https://doi.org/10.1039/c5lc01028d)
- Stucki AO et al (2015) A lung-on-a-chip array with an integrated bio-inspired respiration mechanism. *Lab Chip* 15:1302–1310. doi:[10.1039/c4lc01252f](https://doi.org/10.1039/c4lc01252f)
- Toole BP, Slomiany MG (2008) Hyaluronan: a constitutive regulator of chemoresistance and malignancy in cancer cells. *Semin Cancer Biol* 18:244–250. doi:[10.1016/j.semcancer.2008.03.009](https://doi.org/10.1016/j.semcancer.2008.03.009)
- Voros E et al (2015) TPA immobilization on iron oxide nanocubes and localized magnetic hyperthermia accelerate blood clot lysis. *Adv Funct Mater* 25:1709–1718. doi:[10.1002/adfm.201404354](https://doi.org/10.1002/adfm.201404354)
- Warboys CM, Berson RE, Mann GE, Pearson JD, Weinberg PD (2010) Acute and chronic exposure to shear stress have opposite effects on endothelial permeability to macromolecules. *Am J Physiol-Heart C* 298:H1850–H1856. doi:[10.1152/ajpheart.00114.2010](https://doi.org/10.1152/ajpheart.00114.2010)
- Yeon JH, Na D, Choi K, Ryu SW, Choi C, Park JK (2012) Reliable permeability assay system in a microfluidic device mimicking cerebral vasculatures. *Biomed Microdevices* 14:1141–1148. doi:[10.1007/s10544-012-9680-5](https://doi.org/10.1007/s10544-012-9680-5)
- Zervantonakis IK, Hughes-Alford SK, Charest JL, Condeelis JS, Gertler FB, Kamm RD (2012) Three-dimensional microfluidic model for tumor cell intravasation and endothelial barrier function. *Proc Natl Acad Sci USA* 109:13515–13520. doi:[10.1073/pnas.1210182109](https://doi.org/10.1073/pnas.1210182109)